

Positioning of the rf potential minimum line of a linear Paul trap with micrometer precision

P F Herskind[‡], A Dantan, M Albert, J P Marler and M Drewsen

QUANTOP, Danish National Research Foundation Center of Quantum Optics,
Department of Physics, University of Aarhus, DK-8000 Denmark.

E-mail: drewsen@phys.au.dk

Abstract. We demonstrate a general technique to achieve a precise radial displacement of the nodal line of the radiofrequency (rf) field in a linear Paul trap. The technique relies on selective adjustment of the load capacitance of the trap electrodes, achieved through the addition of capacitors to the basic resonant rf-circuit used to drive the trap. Displacements of up to $\sim 100 \mu\text{m}$ with micrometer precision are measured using a combination of fluorescence images of ion Coulomb crystals and coherent coupling of such crystals to a mode of an optical cavity. The displacements are made without measurable distortion of the shape or structure of the Coulomb crystals, as well as without introducing excess heating commonly associated with the radial displacement of crystals by adjustment through static potentials. We expect this technique to be of importance for future developments of microtrap architectures and ion-based cavity QED.

PACS numbers: 37.10.Ty,37.30.+i,42.50.Pq

[‡] Present address: Research Laboratory of Electronics, Massachusetts Institute of Technology, Cambridge, Massachusetts 02139, USA

1. Introduction

Radiofrequency (rf) traps provide a simple trapping scenario for charged particles [1] and allow for stable confinement for long periods of time [2]. Such traps have proven to be versatile tools for a wealth of investigations, including quantum information science [3], frequency standards [4] and cold molecular ion physics [5].

Due to the time-varying potential inherent in rf traps the trapped ions undergo rapid motion at the applied rf-frequency. This so-called micromotion results in Doppler shifts and broadening of the atomic transitions [6], as well as heating of the ions [7]. Depending on the particular type of trap used, the rf-field may have either a nodal point or a nodal line for which the micromotion vanishes. To avoid excess micromotion and rf-heating of the ions, experiments are often restricted to operate under conditions where the ions reside in these regions, which are typically defined by the trap geometry. This may impose severe demands on the manufacturing and assembly of the trap, should there be a need for the ions to line up with other components incorporated into the trap structure. In microtrap architectures [8, 9] for instance, it might be desirable to integrate optical fibers for cooling, manipulation and detection of the ions [10]. In the field of cavity QED with trapped ions [11, 12, 13], to which this work applies, the ions should be located within the mode volume of an optical resonator, which might only be of the order of $\sim 10 \mu\text{m}$. In both cases a method for displacing the ions with $\sim \mu\text{m}$ precision over tens of μm without inducing an excess of micromotion is therefore of importance to future developments.

One obvious way to achieve this is by physically moving the trap electrodes and, hence, changing the geometric center of the trap, relative to the external objects such as the optical fibers or an optical resonator. In terms of practicality this is, however, not always a viable approach, especially if these objects are integrated into the trap structure. Here, we present a general method for translating the nodal line of a linear Paul trap that does not require any physical translation of any parts of the trap structure and which can be accomplished simply through external adjustments of the rf-circuit residing outside the vacuum chamber. We show that radial displacements of up to $\pm 100 \mu\text{m}$ can be achieved without compromising the trapping of large ion Coulomb crystals and that positioning of the potential minimum with respect to the axis of an optical cavity is possible with micrometer precision.

This paper is organized as follows: In section 2 we review the description of ions in a linear Paul trap. In section 3 we present our scheme for displacement of the nodal line of the rf-field. In section 4 we describe the trap and the technique for measuring the rf-field nodal line position. Section 5 presents results based on two different realizations of the scheme, which are then evaluated and compared against an idealized scenario. In section 6 we perform a characterization of our trap and compare the non-displaced configuration with the displaced one. In section 7 we confirm that the overlap between the potential minimum and the cavity axis is optimal within one micrometer by measuring the coherent coupling strength of prolate ion Coulomb crystals

with the cavity field. Finally in section 8 we conclude.

2. The linear Paul trap

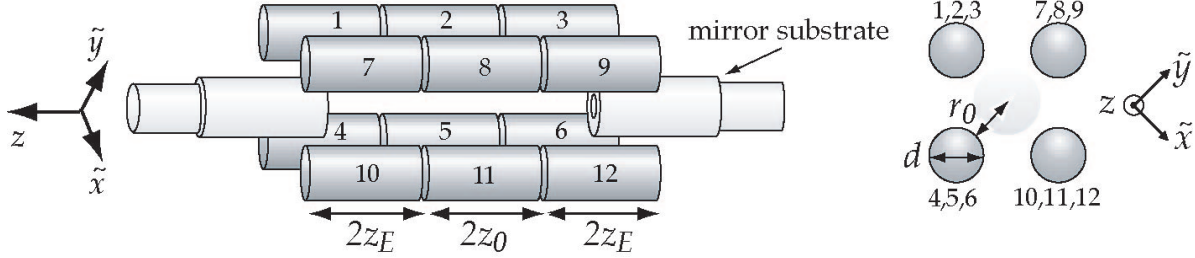


Figure 1. Sketch of the linear Paul trap incorporating an optical resonator. Further details about the trap can be found in [14].

Figure 1 shows a schematic of the linear Paul trap used in the experiments. A special feature of this trap is the integration of an optical cavity into the trap structure with the mirrors located in-between the trap electrodes. This trap has been described in detail elsewhere [14] and here, only a brief review is presented as reference for the remainder of the paper. The trap is operated by applying time-varying voltages $\frac{1}{2}U_{rf}\cos(\Omega_{rf}t)$ to electrodes 1,2,3 and 10,11,12 and $-\frac{1}{2}U_{rf}\cos(\Omega_{rf}t)$ to electrodes 4,5,6 and 7,8,9, where U_{rf} is the amplitude of the rf-voltage and Ω_{rf} is the rf-frequency. This gives rise to a potential in the radial ($\tilde{x}\tilde{y}$)-plane of the form

$$\phi_{rf}(\tilde{x}, \tilde{y}, t) = -\frac{1}{2}U_{rf}\cos(\Omega_{rf}t)\frac{\tilde{x}^2 - \tilde{y}^2}{r_0^2}, \quad (1)$$

where r_0 is the inter-electrode inscribed radius. The sectioning of each of the electrode rods allows for application of a static voltage U_{end} to the end-electrodes, which provides confinement along the z -axis. The electric potential near the center of the trap is then well described by

$$\phi_{end}(\tilde{x}, \tilde{y}, z) = \frac{\eta U_{end}}{z_0^2} \left(z^2 - \frac{\tilde{x}^2 + \tilde{y}^2}{2} \right), \quad (2)$$

where η is a constant related to the trap geometry and $2z_0$ is the length of the center electrodes (2,5,8,11). From the combined potentials of (1) and (2) the resulting motion of a single ion near the center of the trap is described by a Mathieu equation:

$$\frac{\partial^2 u}{\partial \tau^2} + [a_u - 2q_u \cos(2\tau)] u = 0, \quad u = \tilde{x}, \tilde{y}, z. \quad (3)$$

We have introduced the following dimensionless parameters:

$$\begin{aligned} \tau &= \frac{\Omega_{rf}t}{2}, & a_{\tilde{x}} &= a_{\tilde{y}} = -\frac{a_z}{2} = -4\frac{\eta Q U_{end}}{M z_0^2 \Omega_{rf}^2}, \\ q_{\tilde{x}} &= -q_{\tilde{y}} = 2\frac{Q U_{rf}}{M r_0^2 \Omega_{rf}^2}, & q_z &= 0, \end{aligned} \quad (4)$$

where Q and M are the charge and mass of the ion, respectively. The solution to (3) can be written as a Fourier series, from which regions of stable motion can be identified [15]. In general, the trap is operated such that $|a|, |q| \ll 1$, in which case the solution to (3) takes the simple form:

$$u(t) = u_0 \cos(\omega_u t) \left[1 - \frac{q_u}{2} \cos(\Omega_{rf} t) \right], \quad (5)$$

where the secular frequency

$$\omega_u = \frac{\sqrt{q_u^2/2 + a_u}}{2} \Omega_{rf} \quad (6)$$

has been introduced. From (5), two distinct types of motion can be identified: the slow *secular* motion at frequency ω_u and with amplitude u_0 , and the superimposed fast *micromotion* at the rf-frequency Ω_{rf} , which has a much smaller amplitude due to the smallness of the q -parameter. The amplitude of the secular motion is determined by the thermal energy of the ion, which can be minimized, e.g., by Doppler laser cooling.

A constant dc-voltage may also be added to the electrodes in order to create a static electric field in the radial direction. For instance, if applied to electrodes 1,2,3, such a field will shift the location of the potential minimum along \tilde{x} . This modifies the equation of motion as the ion is now displaced from the nodal line of the rf-field by an amount u_{dc} into a region of larger micromotion amplitude. (5) thus becomes

$$u(t) = \left(u_{dc} + u_0 \cos(\omega_u t) \right) \left[1 - \frac{q_u}{2} \cos(\Omega_{rf} t) \right], \quad (7)$$

This means that even for the situation where the secular motion is essentially non-present, the amplitude of the micromotion will still be $\frac{1}{2}u_{dc}q_u$ which may become substantial though the displacement u_{dc} is only of the order of a few microns. This effect, commonly referred to as excess micromotion [6], shows why radial displacement of the ion by application of a static potential is undesirable and motivates an approach based on modification of the potential created by the rf-field.

For large ion clouds, there will always be some ions with equilibrium positions in regions not coinciding with the nodal line of the rf-field and, hence, with large micromotion amplitudes. The transfer of energy associated with their driven motion into random thermal motion, through collisions in the crystal, gives rise to an effective heating rate which has a complex dependence on the trapping parameters, the temperature and the number of ions [16, 17]. This counteracts the Doppler cooling effect and results in temperatures of the ion cloud that are typically a few tens of mK above the Doppler limit [13, 18, 19]. Nevertheless, under good cooling conditions the ions may crystallize to form ion Coulomb crystals and may even exhibit long-range ordered structures [20], expected at temperatures around 10 mK for typical trapping parameters [21].

In less-ideal scenarios, where the equilibrium position of the ion cloud does not coincide with the nodal line of the rf-field, the rf-heating rate can be substantial resulting in inhomogeneous broadening of the atomic transitions and even failure to crystallize due to the high temperature of the cloud. Moreover, this method cannot be used when

working simultaneously with different ion species or isotopes, since the application of a static field fails to maintain the structural symmetry of multi-component crystals [22, 23].

The present paper is focused on general aspects of large ion plasmas and the ability to cool them into ion Coulomb crystals. The persistent structures of these crystals will serve as one figure of merit for the quality of the displacement of the rf nodal line. A specific motivation for this work is cavity QED experiments, where the need for maximizing the overlap between a Coulomb crystal and the cavity modevolume is paramount [13].

3. Moving scheme

For simplicity, we consider the one-dimensional case depicted in figure 2. In the following we shall only analyze the effect of the rf-fields and assume that no offset with respect to the nodal line of the rf-potential has been induced by static fields ($u_{dc} = 0$). Instead, we assume that the rf-amplitude on two electrodes, A and B, can differ by some attenuation factor $\delta < 1$, such that $U_{rf}^B = \delta U_{rf}^A$. The zero-point on the \tilde{x} -axis in figure 2 indicates the location of the geometric center at the distance r_0 from both electrodes. The potential from both electrodes falls off with the inverse of the distance to the electrode and assuming that the displacement is small compared to the trap dimensions ($|\tilde{x}| \ll r_0$), the total potential at \tilde{x} may be written as

$$\phi(\tilde{x}) \propto \frac{U_{rf}^A + U_{rf}^B}{r_0} - \frac{U_{rf}^A - U_{rf}^B}{r_0} \frac{\tilde{x}}{r_0} + \frac{U_{rf}^A + U_{rf}^B}{r_0} \frac{\tilde{x}^2}{r_0^2} + \mathcal{O}\left(\frac{\tilde{x}^3}{r_0^3}\right). \quad (8)$$

Omitting contributions from terms higher than second order, the location of the minimum x_0 is

$$x_0 = \frac{U_{rf}^A - U_{rf}^B}{U_{rf}^A + U_{rf}^B} \frac{r_0}{2} = \frac{1 - \delta}{1 + \delta} \frac{r_0}{2}. \quad (9)$$

For small attenuations ($\delta \approx 1$) one therefore expects the displacement to be linear, $x_0 = (1 - \delta)r_0$, and the potential to remain harmonic around the new minimum. This simple analysis shows that one can lower the amplitude of the rf-voltage on the electrode rod in the direction where we wish to move the potential minimum. The fact that the trap potential retains its harmonic shape (for small displacements) means that the results of section 2 still hold and that the trap should operate normally in the new configuration.

The rf-voltage applied to the trap electrodes in our experiments is supplied by a frequency generator (HP 33120A) and is amplified by an rf-amplifier (Amplifier Research 4W1000) before being transferred to the trap electrodes via a resonant circuit. In this circuit, the trap itself acts as the capacitive part of an LRC-circuit which is inductively coupled to the rf-power supply through a ferrite toroid transformer with a single turn on the source side and 10 turns on the trap side. A diagram of this circuit for the transfer of the rf-voltage to each of the trap electrodes is shown in figure 3. It consists

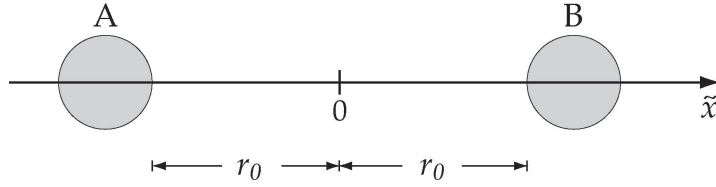


Figure 2. Two electrodes used in the derivation of the location of the shifted potential minimum. See text for details.

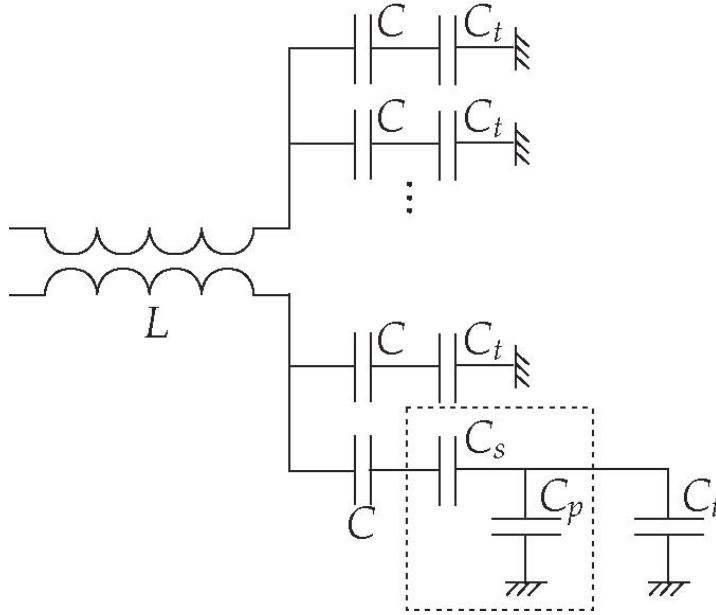


Figure 3. Schematic of the rf resonant circuit. Each electrode is represented by a capacitance C_t . Adjustment of the load on each electrode can be achieved by adding series and parallel capacitances C_s and C_p (see dashed box). This will be treated in detail in section 5.

of two separate circuits with opposite phases, which are created from a single rf-input by winding the output coil wires around the ferrite toroid transformer in opposite directions. Each phase of the rf-voltage is then coupled to a set of six trap electrodes through capacitors C in series. Missing in the figure, is the part of the circuit used to add the dc-voltage to the electrodes, omitted for the sake of simplicity. The electric circuit for each of the electrodes thus consists of a capacitor $C = 2.2$ nF and the trap electrode C_t which, including wires, is typically around 40 pF. The circuit therefore acts as a basic voltage divider and the voltage on one electrode, U_e , with respect to the input voltage, U_{in} , is given by

$$U_e = \frac{U_{in}}{1 + \frac{C_t}{C}}. \quad (10)$$

For our parameters, where $C \gg C_t$, the gain across the voltage divider is close to unity regardless of the exact value of the trap capacitance C_t , which may vary slightly from one electrode to another. Equation (10) shows that lowering the voltage on selected

electrodes can be achieved either by increasing C_t or by decreasing C . In section 5 we will describe how this is done experimentally in both cases. To move the potential minimum radially, we will make identical changes to the capacitive loads on all three electrodes of a given electrode rod (e.g. electrodes 1,2,3 in figure 1).

4. Experimental setup

4.1. Linear Paul trap description

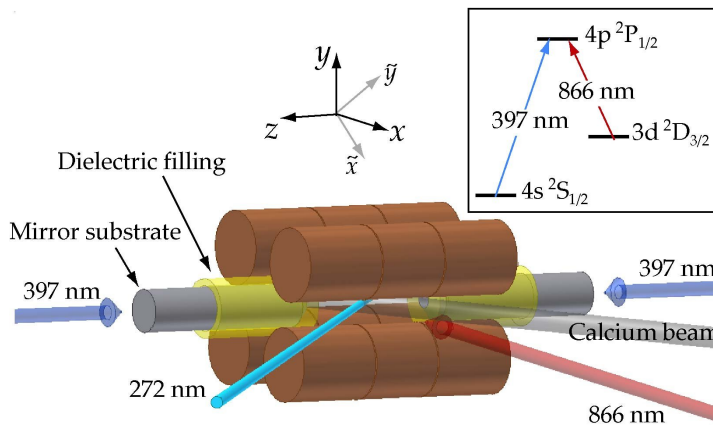


Figure 4. Schematic of the linear Paul trap used in the experiments, along with the beams used for loading and Doppler cooling of the ions. The inset shows the relevant energy levels of the calcium ion for Doppler laser cooling.

The linear Paul trap used in the experiments is shown in figure 4 and has been described in [14]. It consists of four segmented cylindrical rods in a quadrupole configuration. The length of the center electrode is $2z_0 = 5.0$ mm, and the length of the end-electrodes are $2z_E = 5.9$ mm. The electrode diameter is $d = 5.2$ mm and the distance from the trap center to the electrodes is $r_0 = 2.35$ mm (c.f. figure 1). The trap is operated at a frequency $\Omega_{rf} = 2\pi \times 4.0$ MHz and the end- and rf-voltages are typically within the range $U_{end} = 1 - 10$ V and $U_{rf} = 100 - 400$ V, respectively. This corresponds to axial and radial secular frequencies in the range $\omega_z = 80 - 260$ kHz and $\omega_r = 70 - 780$ kHz, respectively, and to ion crystal densities between 6.8×10^7 and 1.1×10^9 cm $^{-3}$. The trap also incorporates a moderately high-finesse cavity ($\mathcal{F} \sim 3000$) in between the electrodes, designed to operate on the $3d \ ^2D_{3/2} \rightarrow 4p \ ^2P_{1/2}$ transition of Ca $^+$ at 866 nm (see insert of figure 4).

The trap is loaded with $^{40}\text{Ca}^+$ and $^{44}\text{Ca}^+$ ions by isotope selective two-photon photoionization [24], by intersecting an atomic beam produced by an effusive oven with a 272 nm beam at the center of the trap. The $^{40}\text{Ca}^+$ ions produced are subsequently Doppler-cooled on the $4s \ ^2S_{1/2} \rightarrow 4p \ ^2P_{1/2}$ transition by two counter-propagating beams at 397 nm along the z -axis, while in the radial (xy)-plane the ions are sympathetically cooled through the Coulomb interaction. An 866 nm beam, propagating along the x -axis and resonant with the $3d \ ^2D_{3/2} \rightarrow 4p \ ^2P_{1/2}$ transition, is applied to prevent the ions

from being shelved into the metastable $D_{3/2}$ state. Detection of the ions is performed by imaging spontaneously emitted light at 397 nm onto two image intensified CCD cameras, monitoring the ions in the (xz) - and (yz) -planes, respectively.

4.2. Measurement scheme with fluorescence images

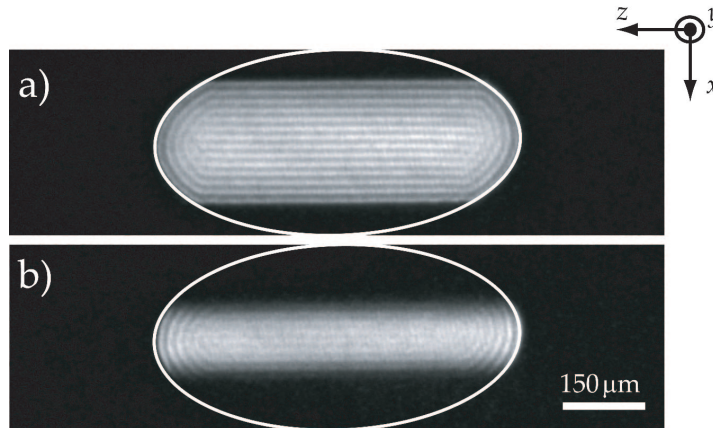


Figure 5. Images of a two-component crystal of $^{40}\text{Ca}^+$ (cooled and visible) and $^{44}\text{Ca}^+$ (outer part, not visible) ions. From image a) to b) the 866 nm repumper is shifted from the beam illuminating the entire crystal from the side (along x) to the cavity mode (along z). The ellipse indicates the outer boundary of the whole $^{40}\text{Ca}^+ + ^{44}\text{Ca}^+$ crystal. Exposure time: 1 s.

We now turn to the measurement of the rf potential minimum line using fluorescence images of the crystals. Because of the isotope selectivity of the photoionization scheme used, it is possible to load simultaneously various isotopes of calcium into the trap [14, 24]. The use of a two-component crystal allows for adjusting the static radial trap potential to coincide with the potential created by the rf-field. Indeed, since the radial secular trap frequency (6) depends inversely on the mass of the ion, heavier ions are confined less tightly in the radial plane. As a result, they appear on the outside of the inner $^{40}\text{Ca}^+$ component. However, this only happens symmetrically if the static potential created by the dc-voltages exactly coincides with the rf nodal line. An example of this is seen in figure 5a), which shows a two-component crystal consisting of $^{40}\text{Ca}^+$ and $^{44}\text{Ca}^+$. Only $^{40}\text{Ca}^+$ is being Doppler laser cooled and visible. The $^{44}\text{Ca}^+$ ions are sympathetically cooled by $^{40}\text{Ca}^+$ ions. The appearance of symmetrical dark regions around the $^{40}\text{Ca}^+$ ions is a signature that the equilibrium location of the ion Coulomb crystal coincides with the nodal line of the rf-field.

Once the dc potential has been adjusted, the repumping light at 866 nm is shifted from the x -axis beam to a beam injected into the cavity (z -axis), the frequency of which is close to resonance with the $3d\ ^2D_{3/2} \rightarrow 4p\ ^2P_{1/2}$ transition. When the repumping light is injected only into the cavity, only the $^{40}\text{Ca}^+$ ions which are located within the cavity mode volume fluoresce, as can be seen from figure 5b). This allows for the detection

of the cavity mode offset with respect to the ion Coulomb crystal center in the plane considered and, therefore, the absolute positioning of the nodal line of the rf-field with respect to the cavity axis.

5. Experimental results

5.1. Addition of a parallel load

In this section we will translate the rf potential minimum line by adding loads on the electrodes. To perform this translation in the (xy) -plane and maintain the symmetry of the trap, the same loads are added to each electrode of a given rod (e.g. 1,2,3). Increasing C_t can be achieved simply by adding a load C_p in parallel, such that $C_t \rightarrow C_t + C_p$ in (10). The attenuation on each electrode is then given by

$$\frac{U'_e}{U_e} = \frac{1 + \frac{C_t}{C}}{1 + \frac{C_t + C_p}{C}} \simeq 1 - \frac{C_p}{C}, \quad (11)$$

assuming $C \gg C_t, C_p$. The expected linear scaling of the rf-field nodal line displacement with increasing value of C_p is confirmed by the results presented in figure 6a). In these measurements, the capacitance C_p was added to either electrodes 1–6 or to electrodes 7–12, as defined in figure 1, thus resulting in a displacement along the x -direction by as much as $\mp 100 \mu\text{m}$. The red line illustrates the linearity of the displacement. A drawback of adding a parallel load, however, is that the resonance frequency of the rf-circuit may be substantially lowered as the load increases. Figure 6b) shows measurements of the resonance frequency of the circuit for various values of the added load C_p . As for the displacement, the effect is symmetric with respect to adding capacitance on either side of the trap. The solid lines are of the form $\frac{1}{\sqrt{a+bC_p}}$, where a and b are free parameters. Lowering the resonance frequency may be undesirable in practice, since, as Ω_{rf} is lowered for the same values of the stability parameters q_u and a_u , the secular frequency as well as the trapping potential will be lowered, which is often unwanted.

5.2. Addition of a series load

As aforementioned, an alternative method consists in adding a capacitor C_s in series (see figure 3). In practice, there is also some coupling to ground associated with this, which is accounted for by the parallel capacitor C_p (~ 10 pF). The attenuation on one electrode thus becomes

$$\frac{U'_e}{U_e} = \frac{1 + \frac{C_t}{C}}{1 + \frac{(C_t + C_p)(C + C_s)}{CC_s}} \simeq \frac{1}{1 + \frac{C_t + C_p}{C_s}} \quad (12)$$

where as previously we have neglected terms according to $C \gg C_t, C_p, C_s$. The resulting displacement is then inversely proportional to the added series capacitance.

The advantage of this method is that it has a comparatively smaller effect on the resonance frequency of the circuit. The combined effect of the added capacitors C_s and

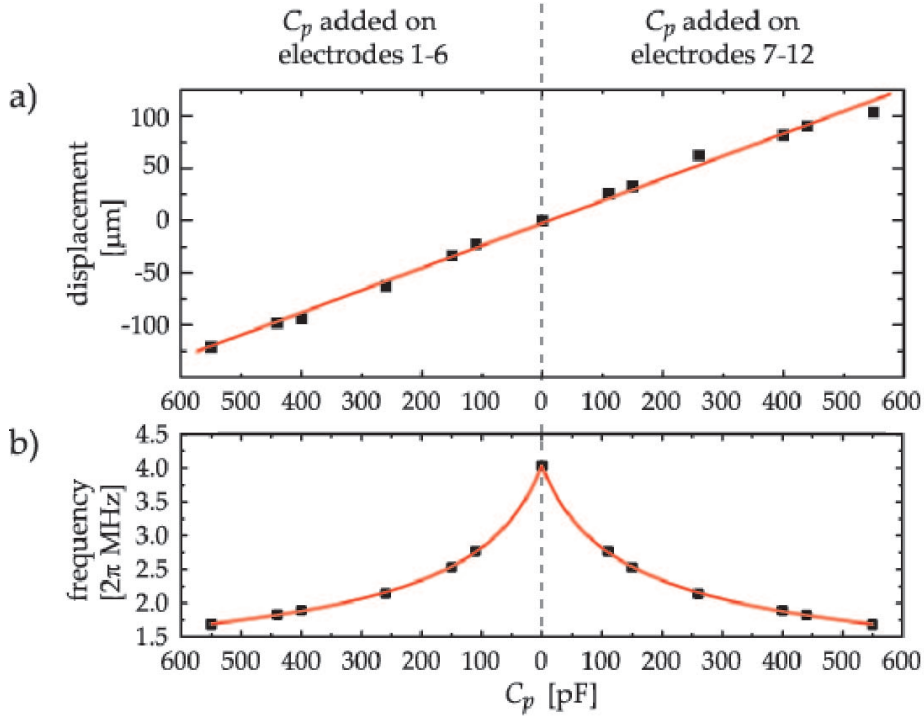


Figure 6. Displacement of the rf-potential minimum found from images of Coulomb crystals by adding a parallel capacitive load C_p on either electrode 1–6 or electrodes 7–12. a) Displacement along the x -direction versus added load and linear fit. b) Resonance frequency of the circuit versus added load. The solid line is of the form $\frac{1}{\sqrt{a+bC_p}}$, where a and b are free parameters.

C_p is to modify the initial electrode capacitance as

$$C_t \rightarrow C'_t = \frac{C_t + C_p}{1 + \frac{C_t + C_p}{C_s}}. \quad (13)$$

The LC-circuit resonance frequency for this electrode will then be modified according to

$$\frac{\Omega'_{rf}}{\Omega_{rf}} \sim \sqrt{\frac{C_t}{C'_t}} = \sqrt{\frac{C_t}{C_t + C_p} + \frac{C_t}{C_s}} \quad (14)$$

Provided that $C_s \gg C_t \gg C_p$, the resonance frequency is therefore expected not to be changed significantly. However, a change, even small, in the resonance frequency for one set of electrodes causes a phase-shift between the two circuits with opposite phase, which may result in increased micromotion [6]. (14) shows that, with a careful adjustment of the loads C_s and C_p , one can keep the resonance frequencies equal for the two circuits. One can therefore ensure that there is no phase-shift between the two circuits with opposite phase after the desired changes in electrode voltages have been obtained.

Figure 7 shows the resulting displacement of a single-component Coulomb crystal for various values of C_s . Black points correspond to the displacement in the x -direction

when C_s is added to electrodes 1–6, while the red points are for displacement in the y -direction when C_s is added to electrodes 1–2–3 and 7–8–9. The solid line is of the form $\frac{1}{C_s}$, applicable to large values of series capacitance for which $C_s \gg C_t, C_p$ (c.f. (12)) and shows nice qualitative agreement.

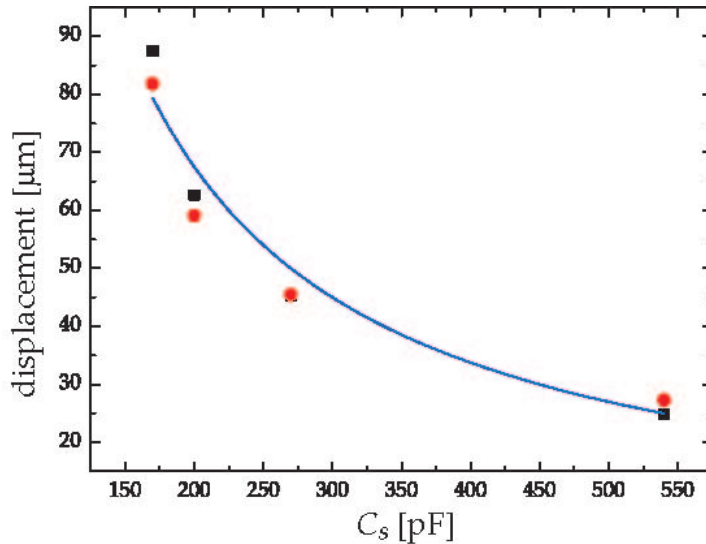


Figure 7. Moving the quadrupole by adding a capacitive load C_s in series. Black squares correspond to the displacement in the x -direction (C_s added to 1–6) while the red circles are for displacement in the y -direction (C_s added to 1–3 and 7–9). The solid line is of the form $\frac{1}{C_s}$.

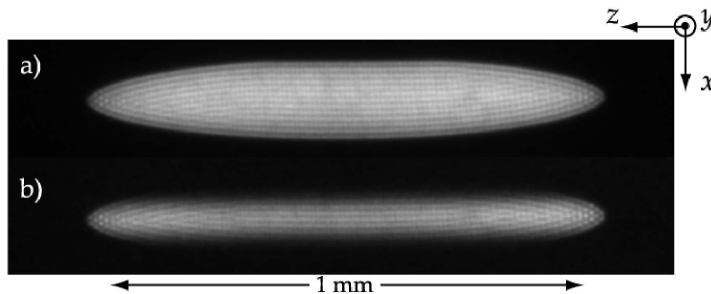


Figure 8. Image of a crystal of $^{40}\text{Ca}^+$ ions in its final position with respect to the cavity mode (adding the set of loads described in section 5.2. From image a) to b) the 866 nm repumper is shifted from the beam propagating along x and illuminating the entire crystal to the cavity mode along z . The rf-field nodal line has been translated by $\sim 90 \mu\text{m}$ in the (xz) -plane, and by $\sim 70 \mu\text{m}$ in the (yz) -plane.

Figure 8 shows an image where the cavity mode is clearly seen. From this image, the overlap between the ion Coulomb crystal and the cavity mode in the (xz) -plane is found to be within $0 \pm 2 \mu\text{m}$. A second camera system along the x -axis is used for detection of the overlap in the (yz) -plane, which is found to be within $0 \pm 8 \mu\text{m}$. Because of the optical resolution the images only provide a crude estimate of the cavity mode

position. A more precise method to determine the overlap between the cavity mode and the crystal center (and therefore the potential minimum) will be presented in section 7.

Combination of loads on all electrode rods ((1,2,3),(4,5,6),(7,8,9) and (10,11,12)) can thus allow for arbitrary positioning of the nodal line of the rf-field anywhere in the (xz)- and (yz)-planes. For the crystal in figure 8 the nodal line has been shifted by $90 \mu\text{m}$ along x and $70 \mu\text{m}$ along y , in order to achieve a near-perfect overlap with the TEM_{00} mode of the optical cavity incorporated into the trap. The formation of highly regular structures indicates that the heating rates and excess micromotion are still low, which is very encouraging for the applicability of the method. Furthermore, at these settings, the observed change in the resonance frequency, compared to the case without any additional load, is 0.3 %. We estimate the phase difference between the rf-fields on electrodes with and without the additional load to be less than 1° and from the model of reference [6] we estimate the resulting excess micromotion to be equivalent to a temperature below 10 mK for typical parameters for our trap. Note that for applications where excess micromotion is a critical issue, one could e.g. adjust the capacitive loads and use the fluorescence modulation technique of [6] to minimize this effect further.

6. Trap characterization

We now turn to a quantitative characterization of the trap parameters and compare the results obtained without any additional load and with the previous set of loads, described in section 5.2, allowing for overlapping the potential minimum and the axis of the optical cavity integrated in the trap.

6.1. Zero-temperature charged liquid model

Both the radial and the axial frequencies are interesting parameters to consider when characterizing the trap. However, as our work is focused on the trapping of large ensembles of ions, we require more information than just the trap frequencies alone, which are typically evaluated from motional excitation spectra of a single or a few trapped ions [25]. Rather, we seek to confirm that the assumption of a harmonic potential, as motivated by our simple model of section 3, is still valid and that it applies over the entire region in space occupied by the ions. To this end, we approximate the trapping potential by a harmonic potential with an axial frequency ω_z (4) and an effective radial frequency equal to the radial secular frequency ω_r given by (6). Based on this assumption, we model the ion plasma as a zero-temperature charged liquid [26], which has previously been shown to be an accurate model for ion Coulomb crystals at temperatures of ~ 10 mK [22]. According to the model one expects the following relation between the ratio of the trap frequencies and the aspect ratio of the crystal,

$\alpha \equiv R/L$, where R is the radius of the crystal and L its axial half-length:

$$\frac{\omega_z}{\omega_r} = \begin{cases} \sqrt{\frac{-2 \frac{\sinh^{-1}(\alpha^{-2} - 1)^{\frac{1}{2}} - \alpha(\alpha^{-2} - 1)^{\frac{1}{2}}}{\sinh^{-1}(\alpha^{-2} - 1)^{\frac{1}{2}} - \alpha^{-1}(\alpha^{-2} - 1)^{\frac{1}{2}}}}{\sinh^{-1}(\alpha^{-2} - 1)^{\frac{1}{2}} - \alpha^{-1}(\alpha^{-2} - 1)^{\frac{1}{2}}}} & , \text{ for } \alpha < 1 \\ \sqrt{\frac{-2 \frac{\sin^{-1}(1 - \alpha^{-2})^{\frac{1}{2}} - \alpha(1 - \alpha^{-2})^{\frac{1}{2}}}{\sin^{-1}(1 - \alpha^{-2})^{\frac{1}{2}} - \alpha^{-1}(1 - \alpha^{-2})^{\frac{1}{2}}}}{\sin^{-1}(1 - \alpha^{-2})^{\frac{1}{2}} - \alpha^{-1}(1 - \alpha^{-2})^{\frac{1}{2}}}} & , \text{ for } \alpha > 1 \end{cases} \quad (15)$$

From (4) and (6) the ratio of the trap frequencies can be written as

$$\frac{\omega_z}{\omega_r} = \sqrt{\frac{-(U_{end} - U_{off})}{\beta(\frac{U_{rf}}{2})^2 + \frac{1}{2}(U_{end} - U_{off})}}, \quad (16)$$

where we have introduced U_{off} to account for any static dc-offsets in the end-voltage U_{end} and where β is defined as

$$\beta = \frac{q_x^2 U_{end}}{a_x U_{rf}^2} = \frac{-Qz_0^2}{M\eta r_0^4 \Omega_{rf}^2}, \quad (17)$$

which for our trap is expected to be $-(2.29 \pm 0.06) \times 10^{-3} \text{ V}^{-1}$, based on the trap parameters [14].

Equating the right hand sides of (15) and (16) we obtain a relation relating the trap parameters to the aspect ratio of the cold trapped crystals that can be used to test the agreement with the zero temperature charged liquid model and to calibrate the trap parameters by treating β as a free parameter. To achieve this, we trap and cool ion Coulomb crystals of $^{40}\text{Ca}^+$ for a large range of trap parameters ($U_{rf} = 100 - 350 \text{ V}$ and $U_{end} = 2 - 15 \text{ V}$) and deduce their aspect ratios α from the recorded images by measuring their radius and length, as described in [27]. From a fit to the data (α versus U_{rf} and U_{end}) we find $\beta = -(2.311 \pm 0.016) \times 10^{-3} \text{ V}^{-1}$, in excellent agreement with our prediction, and $U_{off} = 0.92 \pm 0.05 \text{ V}$, where the non-zero value can be ascribed to charging effects caused by the UV laser during loading or the trap.

To give a visual impression of the validity of the fit and the agreement with the zero-temperature charged liquid model, we use the obtained values for β and U_{off} to calculate $\frac{\omega_z}{\omega_r}$ via (16) and, for each measurement, plot this versus α (red, solid squares in figure 9a)). The solid black line represents the theoretical prediction of (15) based on the zero temperature charged liquid model and is seen to be in good agreement with the data.

Figure 9b) shows the result of a similar measurement after the nodal line of the rf-field has been moved through the addition of serial loads as described in section 5.2. Again, nice agreement with the zero temperature charged liquid model is seen, which supports our arguments in the previous section that the trap potentials should not be distorted by an appreciable amount from their initial harmonic form. From the fit we find $U_{off} = (1.20 \pm 0.03) \text{ V}$ and $\beta = -(2.10 \pm 0.02) \times 10^{-3} \text{ V}^{-1}$. Since only the rf-voltage is modified by our scheme for moving the nodal line, it is expected that the end-voltage U_{end} and the a parameter are unchanged and that the ratio β is modified only as a result

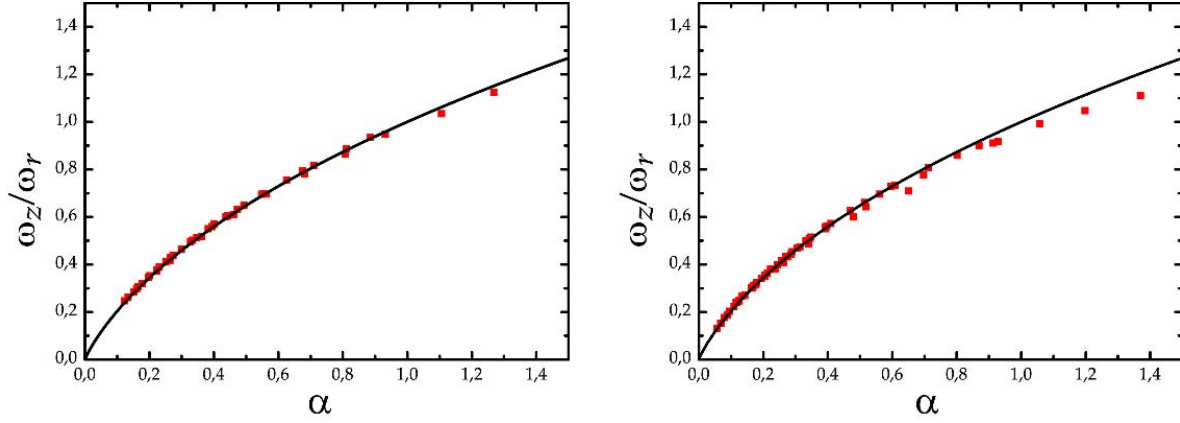


Figure 9. Ratio of trap frequencies versus crystal aspect ratio. a) For no additional load on the trap electrodes. b) For loads added as described in section 5.2. The solid black line is the theoretical curve based on the zero temperature charged liquid model (15) and the red points are data where α has been measured directly from images of crystals and $\frac{\omega_z}{\omega_r}$ has been deduced from a fit to (16). See text for further details. The errorbars are within the point size.

of the attenuation of the rf-voltage. By comparison with the value found without any additional load, we deduce an attenuation factor of 0.96 ± 0.01 .

6.2. Wigner-Seitz radius

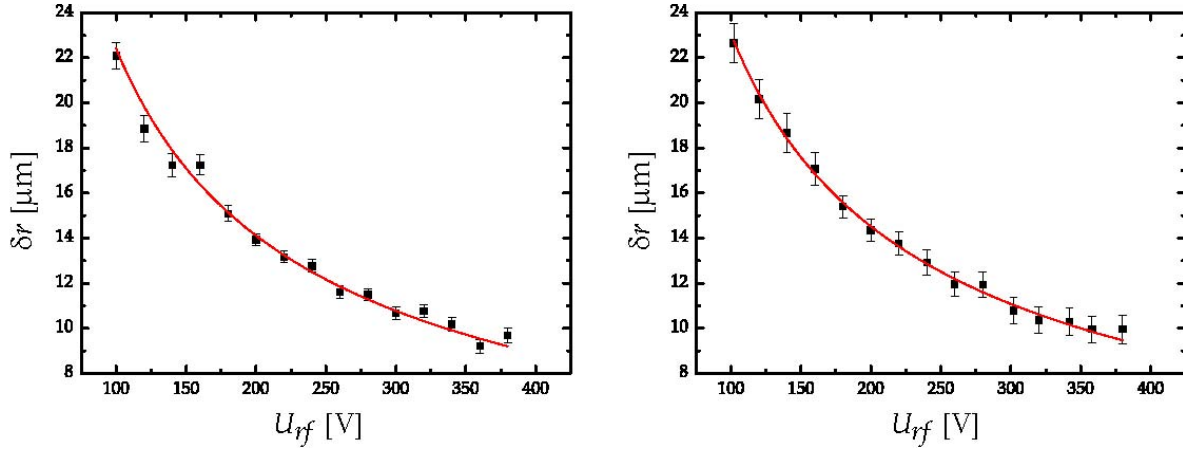


Figure 10. (a) Intershell spacing δr measured as a function of rf-voltage U_{rf} when no additional load is applied to the electrodes. The red line is a fit based on (19) from which the pre-factor is determined to be $\delta_0 = 1.484 \pm 0.010$. (b) δr as a function of U_{rf} when loads are added as described in section 5.2. The red line is a fit based on (19) with $\delta_0 = 1.48$ as a fixed parameter.

For infinitely long crystals of more than three shells, the radial inter-shell spacing δr is predicted by molecular dynamics (MD) simulations to be constant across the crystal and given by the relation [28] $\delta r = 1.48a_{ws}$, where a_{ws} is the Wigner-Seitz radius, defined

as $\frac{4}{3}\pi a_{\text{ws}}^3 = \frac{1}{\rho_0}$. ρ_0 is the average density of crystal, given by [22]

$$\rho_0 = \frac{\epsilon_0 U_{\text{rf}}^2}{M r_0^4 \Omega_{\text{rf}}^2} = \frac{\epsilon_0 \eta}{Q z_0^2} \beta U_{\text{rf}}^2, \quad (18)$$

from which we can express the inter-shell spacing as

$$\delta r = \delta_0 \times \left(\frac{3Qz_0^2}{4\pi\epsilon_0\eta\beta} \right)^{1/3} \times \frac{1}{U_{\text{rf}}^{2/3}}. \quad (19)$$

Here, we have replaced the pre-factor of 1.48 by a fitting parameter δ_0 , which allows us to test the validity of the molecular dynamics simulations for our trap.

Figure 10a) shows the result of measurements of the inter-shell spacing δr for different values of the rf-voltage in the configuration where no additional load has been applied to the electrodes. To mimic the notion of “infinitely long” in the MD simulations, low aspect ratio crystals of 1.5-2 mm length were employed for these measurements. δr is determined from the recorded crystal images as described in [18] and the red line shows the result of a fit to the data based on (19). The fit gives a value for the pre-factor of $\delta_0 = 1.484 \pm 0.010$, which is a significant improvement in the determination of this factor over previous measurements [18] and a strong support of the MD simulations of [28].

A similar set of data has been obtained for the configuration where the serial loads have been added. Figure 10b) shows the results, where for the fit we inserted $\delta_0 = 1.48$ and used β as a free parameter. Again, nice agreement with the model is found and a value of $\beta = -(2.137 \pm 0.045) \times 10^{-3} \text{ V}^{-1}$ is obtained in good agreement with the measurements of the previous section.

7. Overlap between the cavity mode and the potential minimum

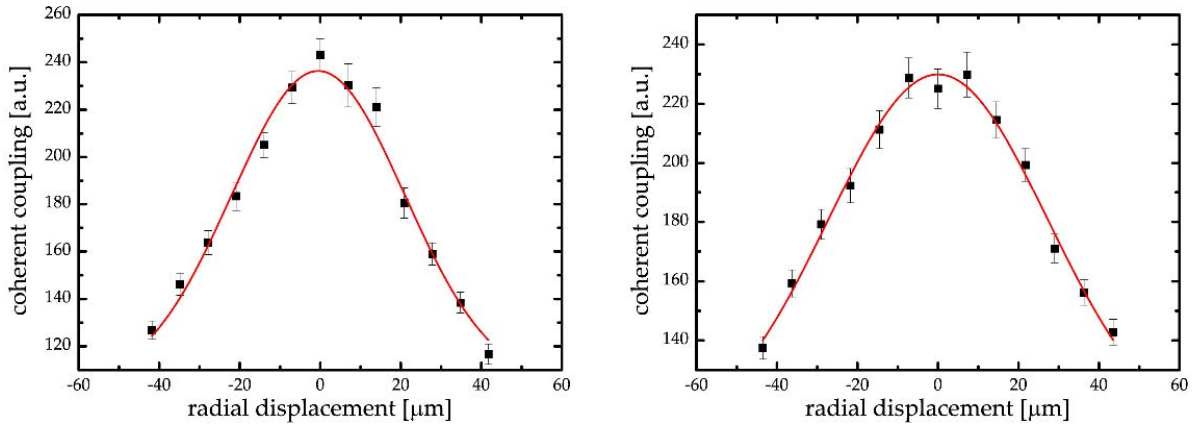


Figure 11. Coherent coupling strength as a function of the crystal radial displacement from the rf nodal line in the (xz) -plane (left) and the (yz) -plane (right). The solid lines are Gaussian fits, yielding horizontal and vertical offsets of $0.0 \pm 0.7 \mu\text{m}$ and $-0.5 \pm 0.5 \mu\text{m}$, respectively.

In order to measure more precisely the overlap between the rf potential minimum and the cavity mode one can make use of the coherent coupling of a thin, prolate crystal with the cavity fundamental TEM_{00} field mode, as demonstrated in [29]. By translating radially a crystal whose radius is smaller than the waist of the cavity and monitoring the change in the coherent coupling strength with the cavity field one can reconstruct the transverse mode profile of the cavity field. We performed similar experiments to those of [29] and translated the ions along the x - and y -axes by application of a suitable static electric field to electrodes (1,2,3) and (4,5,6). The coherent coupling was measured by scanning the cavity length around atomic resonance and injecting a probe field at the single photon level, resonant with the $3d^2D_{3/2} \rightarrow 4p^2P_{1/2}$ transition [13]. Due to the absorption induced by the ions the width of the cavity reflection spectrum is broadened by an amount proportional to the coherent coupling strength, which depends on the overlap between the crystal and the cavity modevolume [29]. Figure 11 shows the variation of the coherent coupling strength with the radial translation of the crystal along two orthogonal axes. The positions of the maxima gives an offset of less than a micrometer of the rf nodal line ($0.5 \pm 0.6 \mu\text{m}$). This confirms the near-optimal positioning of the potential minimum with respect to the axis of the optical cavity.

8. Conclusion

In conclusion we have developed a method for radially translating the rf nodal line of a linear Paul trap based on selective adjustment of capacitive loads on the trap electrodes. Two different methods were analyzed and tested and in both cases the results were well-accounted for by simple models. By appropriate design of the resonant circuit for the rf-voltage, all adjustments can be made outside the vacuum chamber which makes the method attractive from a practical point of view. In the second scheme, adding both parallel and series loads allowed for an arbitrary translation of the potential minimum as well as a precise control of the relative phase between the two rf-circuits and the resonance frequency.

Based on the images of the trapped ion Coulomb crystals, we observed no additional heating effects, caused by excess micromotion, as one would expect, had the ion location been shifted through adjustment of static radial potentials. Furthermore, the validity of both the zero-temperature charged liquid model and the scaling of the inter-shell spacing with the Wigner-Seitz radius, when the position of the ion crystal was shifted, supports the non-invasiveness of the technique. Incidentally, we have found that this analysis provides a value for the pre-factor in the relation between the inter-shell spacing and the Wigner-Seitz radius, with an uncertainty that, to our knowledge, is the lowest obtained thus far, and which is in perfect agreement with MD simulations.

Finally, we employed the coherent coupling between the ion Coulomb crystal and the TEM_{00} mode of the cavity to obtain high-resolution measurements of the location of the crystal with respect to the cavity mode axis. This made it possible to position the ion Coulomb crystal in the cavity mode with a precision at the micrometer level.

We believe this technique will become of high value for cavity QED based ion-photon interfaces and for the development of microtrap architectures for ion-based quantum information science.

Acknowledgments

The authors would like to thank Erik Søndergaard for the development of the original rf-circuit and for useful discussions on the modification of the design. We acknowledge financial support from the Carlsberg Foundation and the Danish Natural Science Research Council through the ESF EuroQUAM project CMMC.

References

- [1] Ghosh P K 1995 *Ion Traps* (New York, Oxford University Press)
- [2] Itano W M, Bergquist J C and Wineland D J 1987 *Science* **237** 612
- [3] Blatt R and Wineland D J 2008 *Nature* **453** 1008
- [4] Rosenband T *et al* 2008 *Science* **319** 1808
- [5] Staannum P F, Højbjerg K, Wester R and Drewsen M 2008 *Phys. Rev. Lett.* **100** 243003
- [6] Berkeland D J, Miller J D, Bergquist J C, Itano W M and Wineland D J 1998 *J. of Appl. Phys.* **83** 5025
- [7] Blumel R, Kappler C, Quint W and Walther H 1989 *Phys. Rev. A* **40** 808
- [8] Stick D, Hensinger W K, Olmschenk S, Madsen M J, Schwab K and Monroe C 2006 *Nature Physics* **2** 36
- [9] Seidelin S *et al* 2006 *Phys. Rev. Lett.* **96** 253003
- [10] Kim J and Kim C 2009 *Quantum Inf. Comput.* **9** 0181
- [11] Guthohrlein G R, Keller M, Hayasaka K, Lange W and Walther H 2001 *Nature* **414** 49
- [12] Mundt A B, Kreuter A, Becher C, Leibfried D, Eschner J, Schmidt-Kaler F and Blatt R 2002 *Phys. Rev. Lett.* **89** 103001
- [13] Herskind P, Dantan A, Marler J, Albert M and Drewsen M 2009, Realization of collective strong coupling with ion Coulomb crystals in an optical cavity, *submitted for publication*
- [14] Herskind P, Dantan A, Langkilde-Lauesen M B, Mortensen A, Sørensen J L and Drewsen M 2008 *Appl. Phys. B* **93**, 373
- [15] Drewsen M and Brøner A 2000 *Phys. Rev. A* **62** 045401
- [16] Schiffer J P, Drewsen M, Hangst J S and Hornekær L 2000 *Proc. Natl. Acad. Sci.* **97** 10697
- [17] Herskind P 2008 *Cavity Quantum Electrodynamics with Ion Coulomb Crystals* (PhD thesis, University of Aarhus)
- [18] Drewsen M, Brodersen C, Hornekær L, Hangst J S and Schiffer J P 1998 *Phys. Rev. Lett.* **81** 2878
- [19] Roth B, Ostendorf A, Wenz W and Schiller S 2005 *J. Phys. B: At. Mol. Opt. Phys.* **38** 3673
- [20] Mortensen A, Nielsen E, Matthey T and Drewsen M 2006 *Phys. Rev. Lett.* **96** 103001
- [21] Pollock E L and Hansen J P 1972 *Phys. Rev. A* **8** 3110
- [22] Hornekær L, Kjærgaard N, Thommesen A M and Drewsen M 2001 *Phys. Rev. Lett.* **86** 1994
- [23] Mortensen A, Nielsen E, Matthey T and Drewsen M 2007 *J. Phys. B: At. Mol. Opt. Phys.* **40** F223
- [24] Mortensen A, Lindballe J J T, Jensen I S, Staannum P, Voigt D, and Drewsen M 2004 *Phys. Rev. A* **69** 042502
- [25] Nägerl H C, Bechter W, Eschner J, Schmidt-Kaler F and Blatt R 1998 *Appl. Phys. B* **66** 603
- [26] Turner L 1987 *Phys. Fluids* **30** 3196
- [27] Hornekær L and Drewsen M 2002 *Phys. Rev. A* **66** 013412
- [28] Hasse R W and Schiffer J P 1990 *Ann. Phys.* **203** 419

- [29] Dantan A, Albert M, Marler J P, Herskind P F and Drewsen M 2009, A multimode ion Coulomb crystal cavity interface, *manuscript in preparation*